Research article

Yeonsang Park*, Hyochul Kim, Jeong-Yub Lee, Woong Ko, Kideock Bae and Kyung-Sang Cho

Direction control of colloidal quantum dot emission using dielectric metasurfaces

https://doi.org/10.1515/nanoph-2020-0158
Received February 29, 2020; accepted May 1, 2020

Abstract: Owing to the recent developments of dielectric metasurfaces, their applications have been expanding from those pertaining to the thickness shrinkage of passive optical elements, such as lenses, polarizers, and quarter-wave plates, to applications pertaining to their integration with active optical devices, such as vertical-cavity surface-emitting lasers. Even though directional lasing and beam shaping of laser emission have been successfully demonstrated, the integration of metasurfaces with random light sources, such as light-emitting diodes, is limited because of function and efficiency issues attributed to the fact that metasurfaces are basically based on the resonance property of the nanostructure. To control the direction of emission from colloidal quantum dots, we present a dielectric metasurface deflector composed of two asymmetric TiO_2 nanoposts. TiO_2 deflector arrays were fabricated with a dry etching method that is adaptive to mass production and integrated with a colloidal quantum dot resonant cavity formed by sandwiching two distributed Bragg reflectors. To ensure the deflection ability of the fabricated sample, we measured the photoluminescence and far-field patterns of emission from the resonant cavity. From the obtained results, we demonstrated that the colloidal quantum dot emission transmitted through our deflector arrays was deflected by 18°, and the efficiency of deflection was 71% with respect to the emission from the resonant cavity. This integration of dielectric metasurfaces with a resonant cavity shows the possibility of expanding the application of visible metasurfaces in active devices and may help to develop next-generation active devices with novel functions.

Keywords: asymmetric nanopost array; colloidal quantum dot; dielectric metasurface; light-emitting diode; resonant cavity; TiO_2 dry etching.

1 Introduction

Metasurfaces are artificial nanostructures that are designed to control the amplitude, polarization, and phase of incident waves at the subwavelength scale [1–4]. Since their emergence in 2011, many researchers have demonstrated that metasurfaces can be used to replace traditional bulky optical components, such as lenses, polarizers, quarter-wave plates, in the form of flat thin-films with thicknesses spanning a few hundred nanometers [5–8]. In addition to passive optical component applications, the applications of metasurfaces to active optical components, such as lasers, light-emitting diodes (LEDs), and quantum light sources, have also been demonstrated in the areas of nonlinear response enhancement of quantum cascade lasers, light–matter interactions, and the control of lasing profiles [9–11]. Because metasurfaces use the resonance properties of nanoantennas, they work well with laser light at a fixed frequency and well-defined wavevectors. Therefore, the combination of metasurfaces with laser devices seems to be natural. In 2018, Ha et al. reported that the control of the lasing direction is possible with the use of a dielectric nanoantenna array [12]. Additionally, Xie et al. demonstrated recently that metasurface axicons that are integrated with the substrate backside of vertical-cavity surface-emitting lasers allow the lasing emission to maintain the beam collimation after it propagates through the substrate [13]. Metasurfaces usually do not work well in the case of LEDs because of the randomness of the LED emission. Therefore, additional mechanisms are required to fix the phase and wavevector of LED emission [14]. In 2017, we presented colloidal quantum dot (CQD) LEDs with nanoslot arrays patterned on their metal electrodes and demonstrated that the polarization and direction of LED emission

Yeonsang Park and Hyochul Kim: These authors contributed equally to this work.

***Corresponding author: Yeonsang Park**, Samsung Advanced Institute of Technology, 130 Samsung-ro, 16678, Suwon, South Korea, E-mail: yeonsang.park@samsung.com. https://orcid.org/0000-0002-9746-8026
Hyochul Kim, Jeong-Yub Lee, Woong Ko, Kideock Bae and Kyung-Sang Cho: Samsung Advanced Institute of Technology, 130 Samsung-ro, 16678, Suwon, South Korea

can be easily controlled by slot-groove arrays because random light that passes through metallic nanoslots has a fixed phase and wavevector [15]. Despite its successful demonstration, the efficiency of LED emission through nanoslot arrays was too low at approximately 4% because of the intrinsic optical loss of the metal and the nanoscale size of slot arrays.

During the past few years, the paradigm of the metasurface study has shifted from plasmonic metasurfaces that are based on metallic nanoantennas to dielectric metasurfaces that use dielectric nanoantennas owing to their increased efficiencies [16–19]. Several research groups reported that the various high-efficiency applications, including holography (efficiency of ~86%), metalenses (efficiency of ≥66%), and spectrometers (efficiency of ~25%), have been achieved with the use of dielectric metasurfaces [20–22]. In addition, directional emission control from the resonant cavity LEDs (RCLEDs) has been demonstrated with the use of Si dielectric metasurfaces [23]. In this work, Si materials with high index (≥ 3.5) were used for the fabrication of visible metasurfaces to achieve 2π phase changes in nanopost structures, despite the fact that Si has very high absorption in the visible range. Therefore, the measured efficiency of fabricated devices was ~3%. To increase the efficiency in the visible range, we present herein CQD RCLEDs integrated with a titanium dioxide (TiO_2) nanopost array as shown in Figure 1. The nanopost arrays were patterned by an inductively coupled plasma reactive-ion etcher (ICP–RIE) that was successfully used in fabricating TiO_2 nanoantenna arrays [24–26]. Based on photoluminescence (PL) measurements and far-field emission images from fabricated RCLEDs, we observed that the emission of RCLEDs was deflected by 18° with an efficiency of 71% with respect to the emission from the resonant cavity.

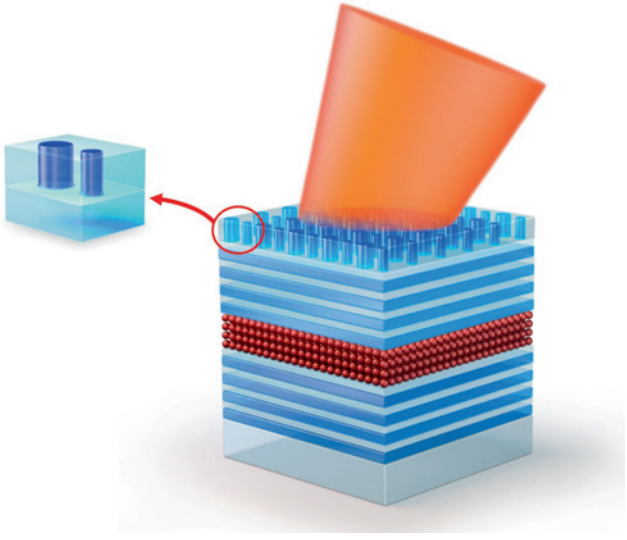

Figure 1: Schematics of a resonant cavity light-emitting diode with TiO_2 metasurfaces.

2 Dielectric deflectors composed of two asymmetric TiO_2 nanoposts

TiO_2 materials are suitable for fabricating visible metasurfaces because they are transparent in the visible range and have a refractive index value of ~2.4 that is higher than that of SiO_2 [27]. However, the refractive index with a value of ~2.4 is not adequately high when compared to the case of high-contrast dielectric metasurfaces. The amplitude and phase of light transmitted through nanopost arrays are determined by the size and period of nanopost arrays. When the phase changes from 0 to 2π range, the transmission of a nanopost can have several dips because of the resonances [28]. If the index contrast between nanoposts and embedded materials is high enough as in the case of Si materials, the metasurface arrays can be properly designed by excluding low transmission conditions because the transmission dip is very narrow. However, for the case of TiO_2 nanoposts, it is more complicated because the index contrast between TiO_2 and embedded SiO_2 is rather moderate. Although thin TiO_2 nanoposts can provide a full phase change in certain conditions, using the TiO_2 nanoposts with thickness above 600 nm is preferred to minimize the abrupt change of phase and transmission, and provides more flexible ranges of the design parameters. Unfortunately, TiO_2 materials cannot be easily deposited at large thicknesses without increasing the extinction coefficient and crystal crack [29]. In addition, it is difficult to etch TiO_2 materials with a high aspect ratio by standard etching techniques, such as the RIE method because of their inherent material hardness [30]. Thus, most TiO_2 metasurfaces are fabricated with the Damascene technique after the atomic layer deposition (ALD) of TiO_2. This renders the mass-production and practical applications of metasurfaces difficult [17, 21]. To avoid this difficulty, Majumdar's group proposed silicon nitride (SiN) materials as another option for visible metasurfaces [27, 31]. Since SiN materials have been major materials in Si technology, they can be fabricated by using a highly-developed complementary metal-oxide-semiconductor (CMOS) fab-technology. Therefore, they are often used in the fabrication of dielectric metasurfaces as well as backbone materials in visible nanophotonics nowadays [32–35]. By contrast, Roh's group used polycrystalline Si materials despite the optical loss in the visible range owing to fabrication compatibilities [36].

We have revisited the use of TiO_2 materials as base materials for visible metasurfaces, and have etched them with ICP–RIE that is compatible with CMOS technology. Figure 2A shows the real (black) and imaginary (red) indices of TiO_2 measured by an ellipsometer. As shown, the real refractive index at a wavelength of 600 nm is 2.4. Additionally, there is no absorption in the region where the wavelength is longer than 390 nm. We etched TiO_2 materials with a thickness of 200 nm by using an e-beam lithography resist (ER) as an etching mask. The scanning electron microscopy (SEM) image of Figure 2B shows that the TiO_2 nanopost arrays with a diameter of 150 nm and a period of 300 nm are fabricated accurately.

For the design of TiO_2 metasurfaces and operation at the wavelength of 600 nm, we calculated the look-up tables (LUTs) of the TiO_2 nanopost with the use of a commercial finite-difference time-domain simulator (FDTD) (Lumerical Inc.). For the calculation of the transmittance and phase changes after the propagation of light through the TiO_2 nanopost, the measured data in Figure 2A were used as the refractive index data of TiO_2, while the medium surrounding the nanopost was set to SiO_2 because the gaps between the nanoposts were filled with SiO_2 for the deposition of reflectors in the fabricated devices. Figure 2C and 2D shows the look-up tables constructed for nanoposts with thicknesses of 700 nm and 300 nm, respectively. Figure 2C shows that a full phase change of 2π can be obtained for a 700 nm-thick TiO_2 nanopost embedded in SiO_2 materials. Since the patterning of TiO_2 nanostructures with a high aspect ratio is quite challenging, we circumvent this difficulty by introducing an alternative design with TiO_2 nanoposts with a low aspect ratio. In this work, we present a dielectric deflector composed of two TiO_2 nanoposts with a thickness of 300 nm which was adapted from the design of the dielectric asymmetric nanoantenna or dimer [24–26].

Figure 3A shows the schematics of a deflector composed of two TiO_2 nanoposts. The deflector structure has a period of 700 nm in the x-direction and a period of 300 nm in the y-direction. One deflector structure consists of two nanoposts with a diameter of 230 and 100 nm. To evaluate the deflecting capacities of the chosen TiO_2 nanoposts, we calculated the transmission spectrum at each diffraction-orders and the scattering far-field patterns by using the FDTD simulator. From the calculated transmission spectrum and deflection angle as a function of the wavelength shown in Figure 3B and 3C, we can see that the transmission with a diffraction-order of one in the x-direction has a value of 0.68 and the deflected angle of this diffraction-order in the x-direction corresponds to 20° at the wavelength of 604 nm. Besides the transmission with a diffraction-order of one, all other transmission amplitudes are suppressed. This implies that TiO_2 asymmetric nanopost arrays can efficiently deflect normal incident light by 20° into the right side (along which the small nanopost is located). To make it sure, we calculated a far-field image at the wavelength of 604 nm with the use of a near-to-far field transformation method and derived ϕ- and θ-polar plot from the obtained far-field as shown in Figure 3D. Based on the

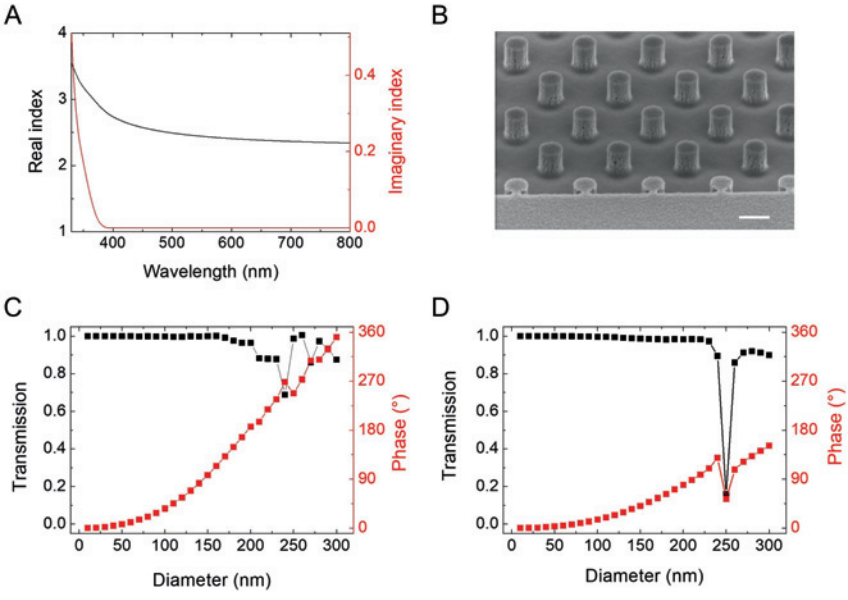

Figure 2: (A) Refractive index of TiO_2 as a function of wavelength measured by an ellipsometer. (B) Scanning electron microscopy (SEM) image of TiO_2 nanopost array patterned by inductively coupled plasma reactive-ion etching (ICP–RIE). The scale bar in the SEM image corresponds to 200 nm. Calculated look-up tables (LUTs) of a TiO_2 nanopost with thicknesses of (C) 700 nm, and (D) 300 nm.

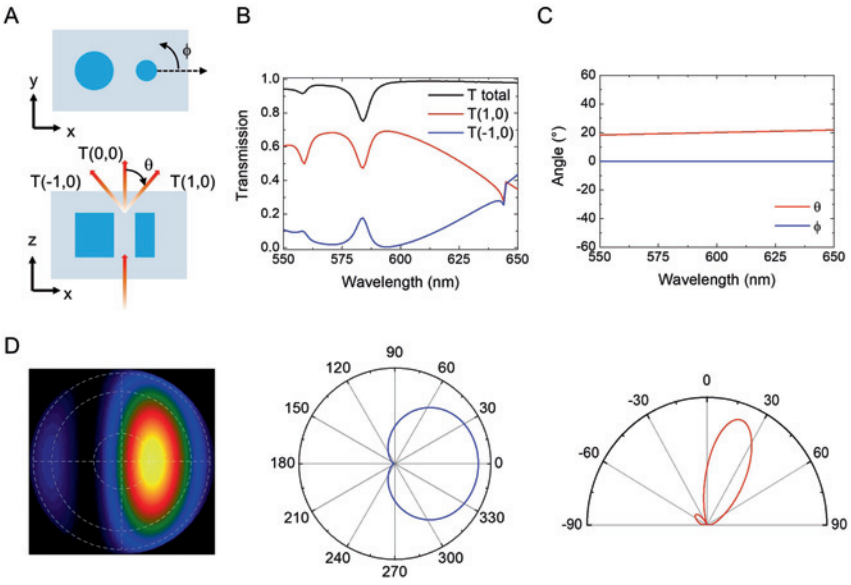

Figure 3: (A) Schematics of a deflector structure. The deflector has a period of 700 nm (300 nm) in the *x*- (*y*-) direction and consists of two asymmetric TiO_2 nanoposts with a thickness of 300 nm. Two nanoposts are embedded in the SiO_2 material. (B) Transmission spectrum with diffraction-order of the deflector unit calculated by the finite-difference time-domain (FDTD) simulator. (C) The calculated deflection angle of transmission with a diffraction-order of 1 as a function of the wavelength. (D) The far-field pattern of the deflector array (left), ϕ-polar plot (middle), and θ-polar plot (right) calculated at the wavelength of 604 nm. White dashed circles in the far-field pattern correspond to the numerical aperture (NA) of 0.3, 0.75, and 0.95 respectively. ϕ-(θ-) polar plot is drawn at the angle θ(ϕ) of the maximum intensity position in the far-field pattern.

simulated results shown in Figure 3, we integrated the dielectric deflector arrays made of two asymmetric nanoposts with the resonant cavity and investigated how the deflector arrays affect the emission from the resonant cavity by measuring the PL spectrum and far-field images. (Supplementary materials S1)

3 Fabrication of TiO_2 nanopost arrays

TiO_2 materials require special attention to be handled with standard CMOS fabrication technology. The deposition of thick TiO_2 film achieved with chemical vapor deposition (CVD) yields crystalline cracks and results in the degradation of the film quality. In addition, dry etching of TiO_2 with RIE is associated with difficulties attributed to the rough profile of the etched structures and the low-etching rate with respect to the soft mask.

In this study, we first deposited TiO_2 materials with a thickness of 300 nm with a sputter, and etched them with an ICP–RIE to fabricate the deflector structure based on the design of two asymmetric TiO_2 nanoposts as shown in Figure 3. Figure 4A shows the entire fabrication procedure of our devices. Nanopost arrays were patterned on the TiO_2 materials with e-beam lithography. The positive tone e-beam lithography resist was used as the etch-mask for patterning of the TiO_2 nanopost. The transmission electron microscopy (TEM) images of the etched TiO_2 nanoposts are shown in the left of Figure 4B. After dry etching, the gaps between the TiO_2 nanoposts were filled with SiO_2 materials with CVD at low pressure. To flatten the surface for the deposition of a distributed Bragg reflector (DBR), we used a chemical mechanical polishing (CMP) method. Accordingly, the flattened surface could be visualized clearly in the magnified TEM image on the right in Figure 4B. Subsequently, we deposited DBRs made of TiO_2 and SiO_2 layers on one substrate integrated with nanopost arrays and another bare quartz substrate simultaneously. The thicknesses of SiO_2 and TiO_2 are 100 nm and 60 nm respectively, and five pairs of SiO_2 and TiO_2 were deposited on two substrates. At the final stage of the sample fabrication, we dropped the CQD solution (which has an emission peak at the wavelength of 604 nm) on the substrate where the DBR was deposited, and the CQD solution was dried at room temperature. To form the resonant cavity of CQDs, we placed the sample integrated with the TiO_2 nanopost arrays upside down on the CQD-coated sample. The thickness of the CQD layer sandwiched by two DBRs was measured as ~5670 nm by calculating the free-spectral range (FSR) of the Fabry–Perot cavity from the measured PL spectra shown in Figure 5B and 5C [37]. (Supplementary materials S2) By measuring the PL and far-field pattern of the fabricated cavity based on the setup shown in Figure 4C, we checked the ability of our designed deflector metasurfaces. Far-field images are measured in the focal length of the convex lens located at the backside of the microscope in the measurement setup. The lens plays the role of Fourier transform upon the incident plane wave, and therefore the

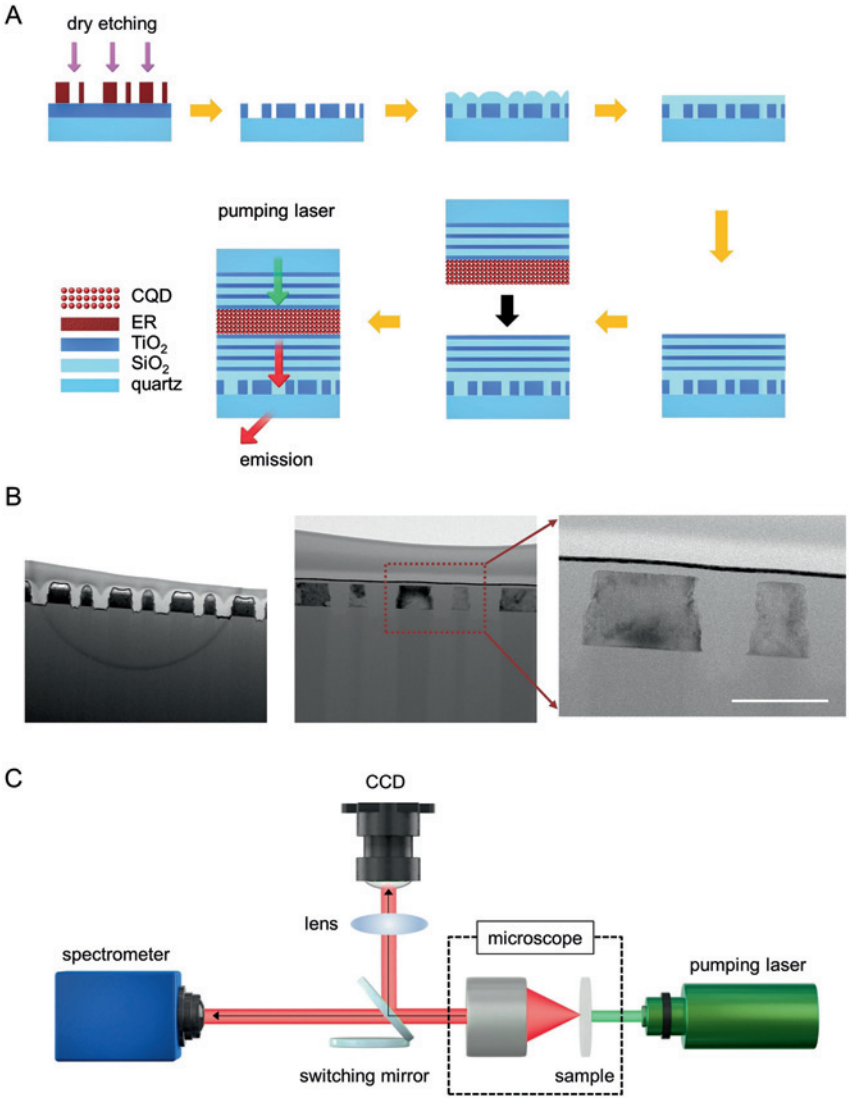

Figure 4: (A) Schematic of the entire fabrication procedure. (B) Transmission electron microscopy (TEM) images of the TiO_2 nanopost arrays etched by ICP–RIE (left), and the two TiO_2 nanoposts flattened by chemical mechanical polishing (right). The scale bar in the right magnified image corresponds to 300 nm. (C) Schematics of PL and far-field pattern measurement setup. By changing the mirror, the optical path can be changed between a spectrometer and the charged-coupled device (CCD).

image obtained in the focal plane of the lens shows the angular distribution of the incident plane wave [15, 34] (Supplementary materials S3).

4 Deflection of emission from the CQD resonant cavity by metasurfaces

We measured the PLs and far-field images of three different samples to find out how the resonant cavity and the integration of the deflector arrays affected the emission of the CQDs. Three schematics in the left column of Figure 5 show three different samples. As a reference, we measured the PL of the emission from the CQDs deposited only on one DBR structure pumped by a laser diode (LD) with a wavelength of 516 nm, as shown in the left of Figure 5A. The measured spectrum shows the representative PL of the red CQD emission with a full-width at half maximum (FWHM) of 33 nm and a peak wavelength of 604 nm. In order to compare the functionality of three different samples, we adapted some parameters that are used in radio frequency (RF) antenna theory. A representative figure of merit associated with the directional antenna is a directivity (D), which is defined as the ratio of the radiation intensity in a given direction to the radiation intensity averaged over all directions [38]. Practically, a directivity can be measured easily by half-power beamwidth (HPBW), which is defined as the angle difference between two opposite points with a half value of the maximum power (Supplementary materials S4). From the

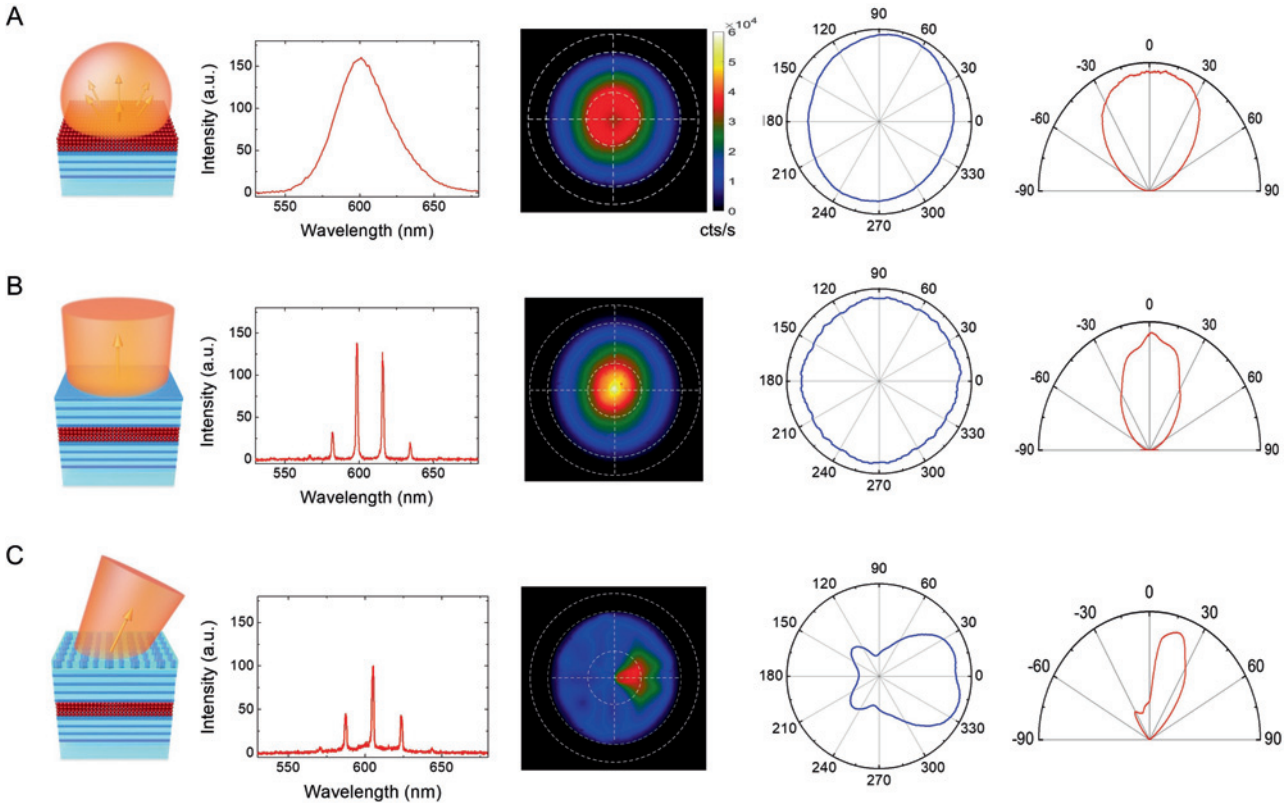

Figure 5: (Left to right) Schematics of the samples, PLs, far-field patterns, ϕ-, and θ-polar plots of the emission from (A) CQDs deposited only on one DBR structure, (B) CQDs sandwiched by two DBRs without a deflector structure, and (C) CQDs sandwiched by two DBRs with a deflector structure. White dashed circles in far-field patterns correspond to NA of 0.3, 0.75, and 0.95 respectively. All far-field images are drawn on the same scale. ϕ-(θ-) polar plot is drawn at the angle $\theta(\phi)$ of the maximum intensity position in the far-field image.

measured far-field pattern, ϕ-, and θ-polar plot as shown in Figure 5A, we can obtain D of ~8.4 at the wavelength of 604 nm and confirm that the emission of the first sample yields a typical far-field pattern of random light sources referred to as Lambertian. The second sample corresponds to the schematics on the left of Figure 5B, and has a CQD resonant cavity formed by sandwiching DBR with the coated-CQD and DBR without the deflector arrays. The measured PL of the second sample shows several peaks with FWHM of 1.27 nm owing to the resonant effect of the cavity. The thickness of the CQD layer is calculated to be ~5670 nm from the FSR of ~17.6 nm. In addition, the directivity at the wavelength of 599 nm (one of the multiple resonance peaks) is measured as ~25.8. Compared with the first sample, the emission from the second sample shows the improved emission directivity with a well-defined wave vector in the normal direction and therefore can be properly coupled with the TiO_2 deflector.

To confirm the effect of the integration with the TiO_2 deflector arrays on the emission pattern from the CQD resonant cavity, we measured the PL and far-field pattern of the third sample that was integrated with TiO_2 deflector metasurfaces, as shown in Figure 5C. Compared with the PL spectrum of the second sample, the wavelengths of the resonant peaks were red-shifted because of the thickness difference of the deposited CQD layers. Additionally, the amplitudes of peaks were decreased because of the reflection at the interface of the deflector metasurface. An FWHM of the peaks is measured as 1.25 nm which is very similar to that of the second sample. This means that the integration of the deflector does not affect the resonance effect of the cavity, and only decreases the efficiency of emission. As shown in Figure 5C, the emission from the CQD resonant cavity with the deflector arrays was deflected by approximately 18° toward the right direction (along which the nanopost with a diameter of 100 nm was located) compared with the far-field of the second sample without the deflector arrays. The measured deflection angle is consistent with the simulated deflection angle of 20°. In addition, the efficiency of the deflection was measured to be 71% with respect to the

second sample. Here, the deflection efficiency was calculated by integrating all intensities inside the HPBW range in measured far-field images of the second and the third samples, and comparing these two values. (Supplementary materials S4) Because of the wide spreading of the emission of the third sample, the D of the third sample is measured as ~9.8 smaller than that of the second one.

5 Conclusions

In conclusion, we presented the design of the deflector composed of two asymmetric TiO_2 nanoposts, and integrated the deflector array composed of dry-etched TiO_2 nanoposts with a CQD resonant cavity. Comparison of the PLs and far-field patterns measured from two CQD resonant cavities with and without the deflector array demonstrated that the fabricated deflector metasurfaces could deflect the emission of the CQD resonant cavity by 18° with an efficiency of 71% with respect to the emission from the resonant cavity.

In the present design, we specifically chose the structure with a limited function in the control of the beam deflection, which did not require a span of full phase change of 2π. To demonstrate the metasurface structures with full control of the far-field pattern, integration of the TiO_2 nanoposts with a high aspect ratio is required. This could be achieved by introducing advanced hard mask materials and etching methods [39]. Instead of using TiO_2 for making the visible metasurfaces, poly-Si or gallium phosphide (GaP) can be good alternatives due to their high refractive index and partial transparency in the visible range [40]. Additionally, using the well-developed deep etching technology in CMOS-fabrication, SiN with enough thickness will be another good candidate material in the visible range [31]. As commented in the introduction section, SiN has a lower refractive index of ~2.0 compared to TiO_2, but an LUT simulation shows that SiN nanoposts with a thickness of 600 nm or more have a full phase change of 2π. Based on the recent rapid developments of visible metasurfaces, we expect that their applications, including their integration with active devices like LDs and LEDs, will continue to expand, and will become an essential and important element in several subfields of nanophotonics.

Author contribution: Y.P. and H.K. designed experiments, fabricated samples and co-wrote the manuscript. Y.P. performed measurements, analysed data and executed simulations. J-Y.L., W.K., K.B., and K-S.C. participated in the sample fabrication. All the authors have accepted responsibility for the entire content of this submitted manuscript and approved submission.

Research funding: None declared.
Employment or leadership: None declared.
Honorarium: None declared.
Conflict of interest statement: The authors declare no conflicts of interest regarding this article.

References

[1] N. Yu, P. Genevet, M. A. Kats, et al., "Light propagation with phase discontinuities: generalized laws of reflection and refraction," *Science*, vol. 334, pp. 333–337, 2011, https://doi.org/10.1126/science.1210713.
[2] A. V. Kildishev, A. Boltasseva, and V. M. Shalaev, "Planar photonics with metasurfaces," *Science*, vol. 339, p. 1232009, 2013, https://doi.org/10.1126/science.1232009.
[3] N. Yu and F. Capasso, "Flat optics with designer metasurfaces," *Nat. Mater.*, vol. 13, pp. 139–150, 2014, https://doi.org/10.1038/nmat3839.
[4] N. Yu, P. Genevet, F. Aieta, et al., "Flat optics: controlling wavefronts with optical antenna metasurfaces," *IEEE J. Sel. Top. Quantum Electron.*, vol. 19, p. 4700423, 2013, https://doi.org/10.1109/aps.2013.6711829.
[5] E. Arbabi, S. M. Kamali, and A. Arbabi, "Faraon A Full-Stokes imaging polarimetry using dielectric metasurfaces," *ACS Photonics*, vol. 5, pp. 3132–3140, 2018, https://doi.org/10.1021/acsphotonics.8b00362.s001.
[6] W. T. Chen, A. Y. Zhu, V. Sanjeev, et al., "A broadband achromatic metalens for focusing and imaging in the visible," *Nat. Nanotechnol.*, vol. 13, pp. 220–226, 2018, https://doi.org/10.1038/s41565-017-0034-6.
[7] S. Wang, P. C. Wu, V.-C. Su, et al., "A broadband achromatic metalens in the visible," *Nat. Nanotechnol.*, vol. 13, pp. 227–232, 2018.
[8] N. Yu, F. Aieta, P. Genevet, M. A. Kats, Z. Gaburro, and F. Capasso, "A broadband, background-free quarter-wave plate based on plasmonic metasurfaces," *Nano. Lett.*, vol. 12, pp. 6328–6333, 2012, https://doi.org/10.1021/nl303445u.
[9] J. Lee, M. Tymchenko, C. Argyropoulos, et al., "Giant nonlinear response from plasmonic metasurfaces coupled to intersubband transitions," *Nature*, vol. 511, pp. 65–69, 2014, https://doi.org/10.1364/cleo_qels.2014.fth4k.1.
[10] P. Rauter, J. Lin, P. Genevet, et al., "Electrically pumped semiconductor laser with monolithic control of circular polarization," *Proc. Natl. Acad. Sci.*, vol. 111, pp. E5623–E5632, 2014, https://doi.org/10.1073/pnas.1421991112.
[11] N. Yu, J. Fan, Q. J. Wang, et al., "Small-divergence semiconductor lasers by plasmonic collimation," *Nat. Photonics*, vol. 2, pp. 564–570, 2008, https://doi.org/10.1038/nphoton.2008.152.
[12] S. T. Ha, Y. H. Fu, N. K. Emani, et al., "Directional lasing in resonant semiconductor nanoantenna arrays," *Nat. Nanotechnol.*, vol. 13, pp. 1042–1047, 2018, https://doi.org/10.1038/s41565-018-0245-5.
[13] Y.-Y., Xie, P.-N. Ni, Q.-H. Wang, et al., "Metasurface-integrated vertical cavity surface-emitting lasers for programmable directional lasing emissions," Nat. Nanotechnol. vol. 15, pp. 125–130, 2020, https://doi.org/10.1038/s41565-019-0611-y.

[14] Z. Liu, E. Khaidarov, Y. Akimov, et al., "Using metasurfaces to control random light emission," in CLEO Pacific Rim Conference 2018. 2018. Hong Kong: Optical Society of America.
[15] Y. Park, J. Kim, K.-S. Cho, et al., "Metasurface electrode light emitting diodes with planar light control," *Sci. Rep.*, vol. 7, p. 14753, 2017, https://doi.org/10.1038/s41598-017-15254-3.
[16] A. Arbabi, Y. Horie, M. Bagheri, and A. Faraon, "Dielectric metasurfaces for complete control of phase and polarization with subwavelength spatial resolution and high transmission," *Nat. Nanotechnol.*, vol. 10, p. 937, 2015, https://doi.org/10.1038/nnano.2015.186.
[17] P. Genevet, F. Capasso, F. Aieta, M. Khorasaninejad, and R. Devlin, "Recent advances in planar optics: from plasmonic to dielectric metasurfaces," *Optica*, vol. 4, pp. 139–152, 2017, https://doi.org/10.1364/optica.4.000139.
[18] S. M. Kamali, E. Arbabi, A. Arbabi, and A. Faraon, "A review of dielectric optical metasurfaces for wavefront control," *Nanophotonics*, vol. 7, pp. 1041–1068, 2018, https://doi.org/10.1515/nanoph-2017-0129.
[19] D. Lin, P. Fan, E. Hasman, and M. L. Brongersma, "Dielectric gradient metasurface optical elements," *Science*, vol. 345, pp. 298–302, 2014, https://doi.org/10.1126/science.1253213.
[20] M. Faraji-Dana, E. Arbabi, A. Arbabi, S. M. Kamali, H. Kwon, and A. Faraon, "Compact folded metasurface spectrometer," *Nat. Commun.*, vol. 9, pp. 1–8, 2018, https://doi.org/10.1038/s41467-018-06495-5.
[21] M. Khorasaninejad, W. T. Chen, R. C. Devlin, J. Oh, A. Y. Zhu, and F. Capasso, "Metalenses at visible wavelengths: diffraction-limited focusing and subwavelength resolution imaging," *Science*, vol. 352, pp. 1190–1194, 2016, https://doi.org/10.1126/science.aaf6644.
[22] W. Zhao, H. Jiang, B. Liu, et al., "Dielectric huygens' metasurface for high-efficiency hologram operating in transmission mode," *Sci. Rep.*, vol. 6, p. 30613, 2016, https://doi.org/10.1038/srep30613.
[23] E. Khaidarov, Z. Liu, R. Paniagua-Domínguez, et al., "Control of LED emission with functional dielectric metasurfaces," *Laser Photonics Rev.*, vol. 14, p. 1900235, 2020, https://doi.org/10.1002/lpor.201900235.
[24] E. Egor Khaidarov, H. Hao, R. Paniagua-Domínguez, et al., "Asymmetric nanoantennas for ultrahigh angle broadband visible light bending," *Nano. Lett.*, vol. 17, pp. 6267–6272, 2017, https://doi.org/10.1021/acs.nanolett.7b02952.
[25] P. Albella, T. Shibanuma, and S. A. Maier, "Switchable directional scattering of electromagnetic radiation with subwavelength asymmetric silicon dimers," *Sci. Rep.*, vol. 5, pp. 18322, 2015, https://doi.org/10.1038/srep18322.
[26] S. Li, X. Xu, R. M. Veetil, et al., "Phase-only transmissive spatial light modulator based on tunable dielectric metasurface," *Science*, vol. 364, pp. 1087–1090, 2019, https://doi.org/10.1126/science.aaw6747.
[27] E. D. Palik, *Handbook of Optical Constants of Solids*, Academic Press, 1998.
[28] A. Zhan, S. Colburn, R. Trivedi, T. K. Fryett, C. M. Dodson, and A. Majumdar, "Low-contrast dielectric metasurface optics," *ACS Photonics*, vol. 3, pp. 209–214, 2016, https://doi.org/10.1364/cleo_at.2016.jw2a.14.
[29] N. Rausch and E. Burte, "Thin TiO_2 films prepared by low pressure chemical vapor deposition," *J Electrochem. Soc.*, vol. 140, pp. 145–149, 1993, https://doi.org/10.1002/chin.199314004.
[30] I. Hotovy, S. Hascik, M. Gregor, V. Rehacek, M. Predanocy, and A. Plecenik, "Dry etching characteristics of TiO_2 thin films using inductively coupled plasma for gas sensing," *Vacuum*, vol. 107, pp. 20–22, 2014, https://doi.org/10.1016/j.vacuum.2014.03.025.
[31] C. Shane, Z. Alan, B. Elyas, et al., "Broadband transparent and CMOS-compatible flat optics with silicon nitride metasurfaces," *Opt. Mater. Express*, vol. 8, pp. 2330–2344, 2018, https://doi.org/10.1364/ome.8.002330.
[32] G. Shilpi and W. Edo, "Spontaneous emission enhancement and saturable absorption of colloidal quantum dots coupled to photonic crystal cavity," *Opt. Express*, vol. 21, pp. 29612–29619, 2013, https://doi.org/10.1364/oe.21.029612.
[33] H. Chang, K. Min, M. Lee, et al., "Colloidal quantum dot lasers built on a passive two-dimensional photonic crystal backbone," *Nanoscale*, vol. 8, pp. 6571–6576, 2016, https://doi.org/10.1039/c5nr08544f.
[34] Y. Chen, A. Ryou, M. R. Friedfeld, et al., "Deterministic positioning of colloidal quantum dots on silicon nitride nanobeam cavities," *Nano. Lett.*, vol. 18, pp. 6404–6410, 2018, https://doi.org/10.1021/acs.nanolett.8b02764.
[35] J. E. Fröch, S. Kim, C. Stewart, et al., "Photonic nanobeam cavities with nanopockets for efficient integration of fluorescent nanoparticles," *Nano. Lett.*, vol. 20, pp. 2784–2790, 2020, https://doi.org/10.1021/acs.nanolett.0c00466.
[36] G. Yoon, D. Lee, K. T. Nam, and J. Rho, "Pragmatic metasurface hologram at visible wavelength: the balance between diffraction efficiency and fabrication compatibility," *ACS Photonics*, vol. 5, pp. 1643–1647, 2017, https://doi.org/10.1021/acsphotonics.7b01044.
[37] M. C. Teich and B. E. Saleh. *Fundamentals of Photonics*, Wiley, pp. 124–127, 1991.
[38] C. A. Balanis. *Antenna Theory: Analysis and Design*, John Wiley & Sons, pp. 42–55, 2016.
[39] F. Laermer and A. Urban, "Challenges, developments and applications of silicon deep reactive ion etching," *Microelectron. Eng.*, vol. 67, pp. 349–355, 2003, https://doi.org/10.1016/s0167-9317(03)00089-3.
[40] J. Y. Lee, Y. Kim, S. Han, et al., "CMOS-compatible Si metasurface at visible wavelengths prepared by low-temperature green laser annealing," *Nanotechnology*, vol. 30, p. 045301, 2018, https://doi.org/10.1088/1361-6528/aaecbd.

Supplementary material: The online version of this article offers supplementary material (https://doi.org/10.1515/nanoph-2020-0158).